Soft Matter

Volume 1 | Number 1 | Jan 2013 | Pages 1–100

Soft Matter

www.rsc.org/softmatter

ROYAL SOCIETY OF CHEMISTRY

This is an *Accepted Manuscript*, which has been through the Royal Society of Chemistry peer review process and has been accepted for publication.

Accepted Manuscripts are published online shortly after acceptance, before technical editing, formatting and proof reading. Using this free service, authors can make their results available to the community, in citable form, before we publish the edited article. We will replace this *Accepted Manuscript* with the edited and formatted *Advance Article* as soon as it is available.

You can find more information about *Accepted Manuscripts* in the **Information for Authors**.

Please note that technical editing may introduce minor changes to the text and/or graphics, which may alter content. The journal's standard **Terms & Conditions** and the **Ethical guidelines** still apply. In no event shall the Royal Society of Chemistry be held responsible for any errors or omissions in this *Accepted Manuscript* or any consequences arising from the use of any information it contains.

ROYAL SOCIETY OF CHEMISTRY

www.rsc.org/softmatter

ARTICLE TYPE

Membrane Indentation Triggers Clathrin Lattice Reorganization and Fluidization

Nicholas Cordella,[a] Thomas J. Lampo,[a] Nicholas Melosh,[b] and Andrew J. Spakowitz[a,b,c]

Clathrin-mediated endocytosis involves the coordinated assembly of clathrin cages around membrane indentations, necessitating fluid-like reorganization followed by solid-like stabilization. This apparent duality in clathrin's *in vivo* behavior provides some indication that the physical interactions between clathrin triskelia and the membrane effect a local response that triggers fluid-solid transformations within the clathrin lattice. We develop a computational model to study the response of clathrin protein lattices to spherical deformations of the underlying flexible membrane. These deformations are similar to the shapes assumed during intracellular trafficking of nanoparticles. Through Monte Carlo simulations of clathrin-on-membrane systems, we observe that these membrane indentations give rise to a greater than normal defect density within the overlaid clathrin lattice. In many cases, the bulk surrounding lattice remains in a crystalline phase, and the extra defects are localized to the regions of large curvature. This can be explained by the fact that the in-plane elastic stress in the clathrin lattice are reduced by coupling defects to highly curved regions. The presence of defects brought about by indentation can result in the fluidization of a lattice that would otherwise be crystalline, resulting in an indentation-driven, defect-mediated phase transition. Altering subunit elasticity or membrane properties is shown to drive a similar transition, and we present phase diagrams that map out the combined effects of these parameters on clathrin lattice properties.

1 Introduction

Clathrin is an essential component of the common intracellular trafficking mechanism known as clathrin-mediated endocytosis (CME)[1,2]. During CME, intracellular cage-like clathrin lattices stabilize highly curved membrane buds that grow into vesicles as they engulf associated cargo[3–6]. The majority of these clathrin-coated vesicles (CCV's) originate through coordinated piecewise assembly of clathrin and their adaptor proteins into curved clathrin-coated pits[7] that close off into spherical cages. However, large, distinct flat clathrin assemblies known as "plaques" are also observed on cell membranes[8–10], with experimental visualizations and physical models raising the possibility that some CCV's may bud off of these larger structures[11–15]. Transport *via* CME is crucial for eukaryotic organism survival[16–18], with aberrations linked to the spread of pathogens[19], growth of cancer[20], and protein conformational diseases[21]. Understanding the physical transformations central to the endocytic pathway is therefore vital for developing technology that enables efficient intracellular transport of biomolecules.

Recent investigations have demonstrated enhanced biomolecular transport near regions of the cell membrane that are locally impinged by surface-modified nanowires[22]. The precise mechanisms behind this efficient delivery method are unclear. Theoretical and experimental models have demonstrated that this phenomenon does not often result from direct penetration of the cell membrane[23,24]. Instead, we propose that locally enhanced CME results from a physical mechanism that enables clathrin rearrangement near the highly curved regions at which the cell membrane is closely adhered to the nanowires.

In this work, we present a physical model of clathrin proteins on a fluctuating membrane to explore the influence of local deformations on the thermodynamic behavior of the lattice. Our computational model demonstrates that profound changes in the architecture and bulk phase of clathrin lattices can be induced by local membrane curvature comparable to early wrapping profiles around nanowire indentation or extracellular cargo. By conducting Monte Carlo simulations of protein lattices associated to such membrane deformations, we observe localization of defects and even a crystalline-fluid melting transition over length scales much larger than the indented region. The insertion of defects and facile adjustment of subunits are important criteria for successful formation of endocytic vesicles. Therefore, these findings point to a previously unconsidered driving force behind CME, in which

[a] *Department of Chemical Engineering, Stanford University, Stanford CA 94305, USA.*
[b] *Department of Materials Science and Engineering, Stanford University, Stanford CA 94305, USA.*
[c] *Biophysics Program, Stanford University, Stanford CA 94305, USA.*

wrapping-induced curvature physically enables the clathrin lattice reorganization necessary for vesiculation. This phenomenon is distinct from the prevailing theories that assume the protein coat is both driving and stabilizing the initial curvature of the membrane, and it explains recently observed enhanced biomolecular uptake on nanowire arrays[22].

2 Model Description

Clathrin Model. In this work, we employ our previously published coarse-grained physical model for clathrin triskelia on a flexible membrane[25], with each triskelion represented by a three-legged pinwheel. This simplification with respect to the actual ∼650 kDa heterohexameric structure[26,27] allows us to capture relevant assembly behavior over realistic computational time frames[25,28,29]. In its ground state, the three straight legs of length r_0 are symmetrically distributed around the central hub and oriented so that a vector from hub i to the end of each leg forms a pucker angle $\alpha_0 = 101°$ with the vector $\vec{n}_i$, which is normal to the plane that is shared by the end of the three legs. This degree of puckering is slightly smaller than that which is inferred from dynamic light scattering of individual triskelia[30] and cryomicroscopy of *in vitro* cages[27,31], but larger than that which would be compatible with the typical sizes of *in vivo* cages[32].

Each leg is capable of binding to one leg on another pinwheel, resulting in an energetic benefit of $-\varepsilon$. Deviations from the ground state configuration of the pinwheel legs contribute deformation energies through four harmonic elastic modes. Stretching or compressing the legs from their equilibrium length r_0 is mediated by the stretching modulus k_s. The twisting modulus k_t controls the ability of neighboring bound hubs i and j to twist their normal vectors $\vec{n}_i$ and $\vec{n}_j$ out of alignment. Deviations to the symmetrical in-plane angular separation of $120°$ between legs is modulated by the in-plane bending modulus k_b, and out-of-plane bending away from α_0 is controlled by the out-of-plane bending modulus k_o. Throughout all simulations in our study, we set all elastic moduli to a constant ratio, such that $k_o = k_b = k_t = k_s r_0^2/10$, which roughly approximates the relative stiffness of these modes as detected experimentally[33]. To avoid steric overlap in our model, we include a short-range repulsive term that scales as r_{ij}^{-4} for separation r_{ij} between hubs i and j. The magnified inset of Fig. 1 illustrates the elastic deformation modes of a single triskelion bound within an interconnected lattice. Appendix A includes a detailed mathematical description of the elastic clathrin model.

Membrane Model. Our model cell membrane is a continuous, periodic elastic sheet, which is appropriate for the size of deformations in this work[34–36]. We employ a Monge representation, defining the membrane configuration with a single-valued height field $h(\vec{\rho})$ that gives the displacement of
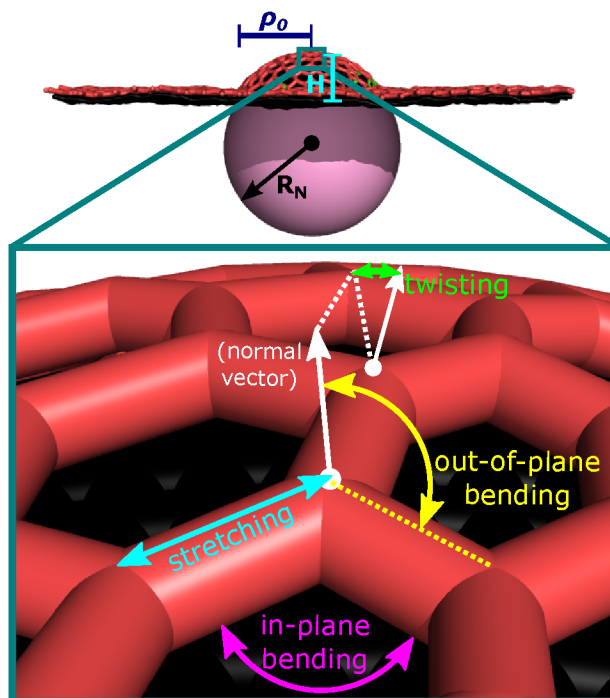

Fig. 1 Side view of our simulated system. The clathrin protein is shown in red, assembling on a black membrane, with a fractional indentation of $f = 0.45$ around a nanoparticle of $R_N = 10r_0$ ($H = 4.5r_0$). The zoomed-in view labels the different deformation modes of a clathrin hub.

the membrane from some reference value in the z-direction at the position $\vec{\rho}$ in the x-y plane. A bending modulus κ resists membrane curvature, and a tension σ resists the generation of surface area. The membrane energy is given by the Canham-Helfrich Hamiltonian[37–39]

$$E_{mem} = \int_A d\vec{\rho} \left\{ \frac{\kappa}{2} \left[\nabla^2 h(\vec{\rho}) \right]^2 + \frac{\sigma}{2} \left[\vec{\nabla} h(\vec{\rho}) \right]^2 \right\}, \quad (1)$$

over the projected area A in the x-y plane. This formulation is valid for deformations that cause only small gradients in $h(\vec{\rho})$. The membrane is discretized as a rectangular mesh with a spacing of $r_0/4$ between grid points in the x-direction and an equal number of grid points in the y-direction. The gradient and Laplacian terms in Eq. 1 are calculated using first- and second-order central difference formulas, respectively.

As illustrated in Fig. 1, we fix a portion of the membrane to a portion of a spherical model nanoparticle with radius $R_N = 10r_0$, roughly corresponding to an outer vesicle diameter of 320 nm, if the inter-hub strut distance is taken to be 320 nm[32]. This is two to three times as large as most vesicles formed *via* CME in living cells[40,41] but considerably smaller than those surrounding certain types of bacteria, fungi and viruses[42–45]. Our simulated nanoparticles are therefore intermediate in size

between the physiologically relevant benchmarks of canonical pits and large pathogens.

The membrane in this indented region adopts a spherical cap shape of height H, which is defined by the fractional indentation $f \equiv H/R_N$. Because larger indentations lead to sharper deformations of the membrane, our small gradient approximation shown in Eq. 1 will significantly deviate from the exact solution at large values of f. Previous studies have shown that there is a marked discrepancy when the indentation approaches $f = 0.5$ at tensions smaller than those examined in the current manuscript[46,47], but the difference between the approximate and exact solutions will be smaller at the relatively large tensions that we explore. An exact solution would also lead to greater membrane curvatures surrounding the nanoparticle, further encouraging the curvature-driven effects on the protein lattice that are highlighted in this manuscript. We therefore apply this small gradient approximation to indentations as large as $f = 0.45$, as it provides a conservative estimate of the degree of curvature that membrane-bound lattices may experience near nanoscale indentations.

The sphere is centered within our periodic cell in the x-y plane and has a center of mass at a vertical location $H - R_N$ relative to the lowest point of membrane-sphere contact, called the "detachment point". The detachment radius ρ_0 in the x-y plane, outside of which membrane points are free to fluctuate, is given by $\rho_0 = R_N \sqrt{2f - f^2}$. All membrane points within the detachment radius are in direct contact with the sphere surface and are accordingly not subject to thermal fluctuations throughout our simulations.

We examine 2 finite tensions, $\sigma = 1.9 k_B T / r_0^2$ and $\sigma = 19 k_B T / r_0^2$, where $k_B T$ is the thermal energy. This range encompasses a large portion of physiologically observed tensions[48]. We also test membranes at infinite tension that exhibit a nanoparticle deformation but no out-of-plane thermal fluctuations. The bending modulus of our membranes is held constant throughout the simulations at $\kappa = 4.7 k_B T$. These physical properties, along with the degree of nanoparticle indentation, dictate the ground state configurations of our model systems. Appendix B provides the mathematical derivation of the membrane ground state configuration.

These nanoparticle-driven deformations can result in significant changes to the surface area of a membrane within the boundaries of constant dimensions in the x- and y-coordinates. To mitigate density-based phenomena in our simulations, we adjust the boundaries of the periodic cell so the surface area of the ground state membrane configuration is the same ($A_s = 2562 r_0^2$) at all tensions and indentations. We use a constant number of clathrin ($N = 1972$) in our simulations, corresponding to the density of a condensed, perfectly ordered lattice when laid on a flat, nearly square periodic membrane of area $A_s = 51 r_0 \times 50.23 r_0$. Appendix B has details of how we make our adjustments to the boundaries of our periodic cell. The

clathrin are coupled to the membrane by fixing their z-position to the height of the nearest membrane grid point. Throughout the thermodynamic simulations, the clathrin are free to move in the x-y plane, and upon each translocation their z-position is adjusted accordingly.

Simulation Methodology. We conduct Monte Carlo (MC) simulations using the Metropolis algorithm that determines the probability of accepting each attempted move according to a Boltzmann weighting[49]. The three types of moves of our MC simulation are membrane motion, clathrin motion, and clathrin binding. We employ an adaptive step-size algorithm to maintain roughly 50% acceptance of the steps that move the clathrin position or change the membrane shape. Each Monte Carlo simulation is started out with the membrane in its ground state irrespective of the clathrin lattice. A fully-satisfied honeycomb lattice is overlaid on this membrane, with bond connectivity that is identical to the ground state on a flat sheet and compressed proportionally with the cell boundaries in the x- and y- directions. For the first 2 million steps of the simulation, we allow the membrane and clathrin hub locations to thermalize without incorporating binding attempts. This avoids unbinding events that are driven by the unnaturally contorted starting configuration of the hubs near highly curved regions of the membrane. We run the simulations for 8 billion total steps, with each step including six membrane moves, a single clathrin move and a single binding move. Six repeats of these stochastic simulations for each parameter set are conducted.

3 Results

Large, ordered clathin lattices, also known as plaques, are observed in many experimental visualizations[10,50,51] and in our previously published simulations[25,28]. We characterize plaques as two-dimensional crystals based on their long-range orientational ordering of six-sided rings formed by their interlocking legs. The most typical defects in these crystalline structures are composed of five- and seven-sided rings. A lone non-six-sided ring represents a disclination, while a five-sided ring and a seven-sided ring closely coupled to one another represent a dislocation. Defects arise in the crystalline phase as a result of thermal fluctuations. However, they are constrained to exist as tightly coupled dislocation pairs, and the elastic strain on the surrounding lattice is minimal.

The melting of a crystalline phase into a fluid phase is characterized by the prevalence of uncoupled dislocations and disclinations[52–54]. Unlike dislocation pairs, these defects impart distortions on the surrounding lattice region and result in the decay of orientational order over short length scales. The initial detailed theory supporting defect-mediated melting phenomena in two dimensions was developed by Kosterlitz, Thouless, Nelson, Halperin and Young (KTHNY The-
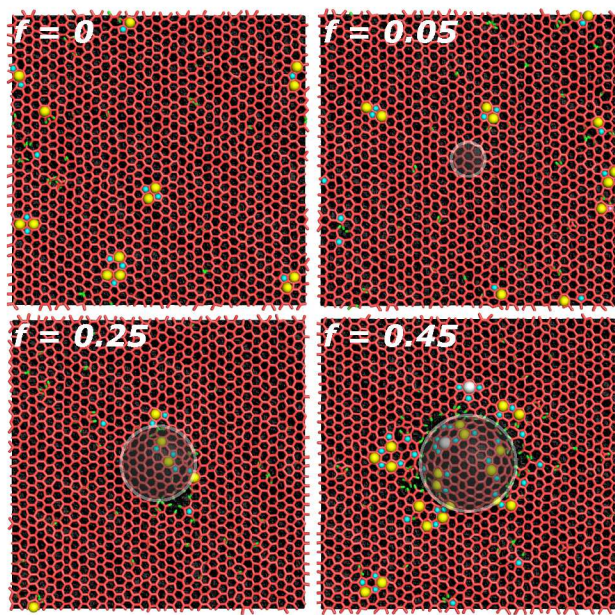
Fig. 2 Representative overhead snapshots of clathrin lattices on membranes subject to varying degrees of fractional indentation f by the model nanoparticle. Clathrin hubs and bound legs are red, while unbound legs are green. Five-sided rings are highlighted with cyan circles, seven-sided rings are highlighted with yellow circles, and eight-sided rings are highlighted with white circles. The shadowed circular regions identify the portion of the membrane that is fixed to the surface of the spherical indentation.

ory)[52–54]. We demonstrate in our previous work that both high clathrin subunit elasticity[28] and high membrane tension[25] stabilize crystalline clathrin phases. It is also clear from experimental evidence[32,51] and topological constraints[55] that curved pits and vesicles require lone pentagonal disclinations. In this work, we address the impact of spherical cap-like indentations on the bulk phase and defect arrangement in lattices that would otherwise be very crystalline in the absence of indentations (*i.e.* the "quasiflat" condition).

Figure 2 shows representative snapshots of our system at varying degrees of indentation. In this case, the membrane has a tension of $19k_BT/r_0^2$ and a clathrin stretching modulus of $92.5k_BT/r_0^2$, which is deep within the quasiflat crystalline phase. This chosen stiffness is within an order of magnitude of rough estimates extracted from representative electron micrographs of clathrin[33,56]. Closed ring defects of between four and eight sides are highlighted by colored spherical markers for ease of interpretation. Without any membrane indentation ($f = 0$), most of the defects exist as dislocation pairs, and they are not localized to any particular region within the crystalline, predominantly honeycomb lattice. At very shallow indentation ($f = 0.05$), the membrane is essentially pinned to a very small spherical cap of the nanoparticle, of radius $\rho_0 \approx 3$ and

an enforced out-of-plane deformation that is similar in scale to the undulations caused by thermal fluctuations. The general distribution of defects at $f = 0.05$ is indistinguishable from the case of $f = 0$.

Once larger indentations of $f = 0.25$ and $f = 0.45$ are introduced, the number of defects in the lattice increases. They are more diverse in nature, not restricted to the low-energy dislocation pair configuration, and most of them are localized to regions near the indentation. This is most noticeable in the case of the void spaces. These void spaces are localized to just outside the circular perimeter of radius ρ_0, within which the membrane is fixed to the spherical surface of the nanoparticle. Figure 2 illustrates a typical configuration, with the voids taking the form of patches that are a few clathrin leg lengths in diameter. A similar dearth of hubs and localization of ring defects is further accentuated at large indentations ($f = 0.45$). The voids in this case tend to form persistently disconnected scars in a circular pattern around the large indentation. The clathrin in the center of the large indentation are connected to the bulk lattice, but often through bridges of connectivity that are often defect-ridden themselves.

Because triskelia are all identical within each simulation, any defect localization is related to a configurational property of the membrane itself that translates a stress to the locally coupled clathrin. The exact shape of our membranes vary *via* random fluctuations around an average configuration that is close to the analytical ground state described in Appendix B. Fluctuations are completely suppressed on the nanoparticle, but outside of the detachment point they grow in magnitude to a uniform size that is solely dependent on the membrane's physical properties. The relatively small fluctuations near the detachment point are likely not responsible for void space localization in that region, because the fluctuations are much larger in the bulk surrounding area, where void spaces are minimal.

In contrast, the Gaussian curvature K and mean curvature M exhibit sharp peaks in the region immediately surrounding the sphere. Figure 3 shows the analytical forms of K and M in the membrane ground state as a function of distance from the nanoparticle center, for $\sigma = 19k_BT/r_0^2$. At all indentations, there is an abrupt negative (positive) peak in Gaussian (mean) curvature immediately outside the detachment point. The peak in K has roughly the same magnitude at all indentations, but the peak in M is noticeably larger at $f \geq 0.25$ than at $f = 0.05$. Curvature peaks persist over a larger region at greater indentations, spanning a couple of clathrin leg lengths at most. This results in the curvature profoundly affecting the clathrin configuration in a narrow ring surrounding the detachment point at indentations greater than $f = 0.25$. Lower tension membranes exhibit smaller peaks in curvature. Due to their preferred 101° pucker angle, the model clathrin subunits have an innate positive curvature of $K_c = 0.15r_0^{-2}$ and a negative mean curvature
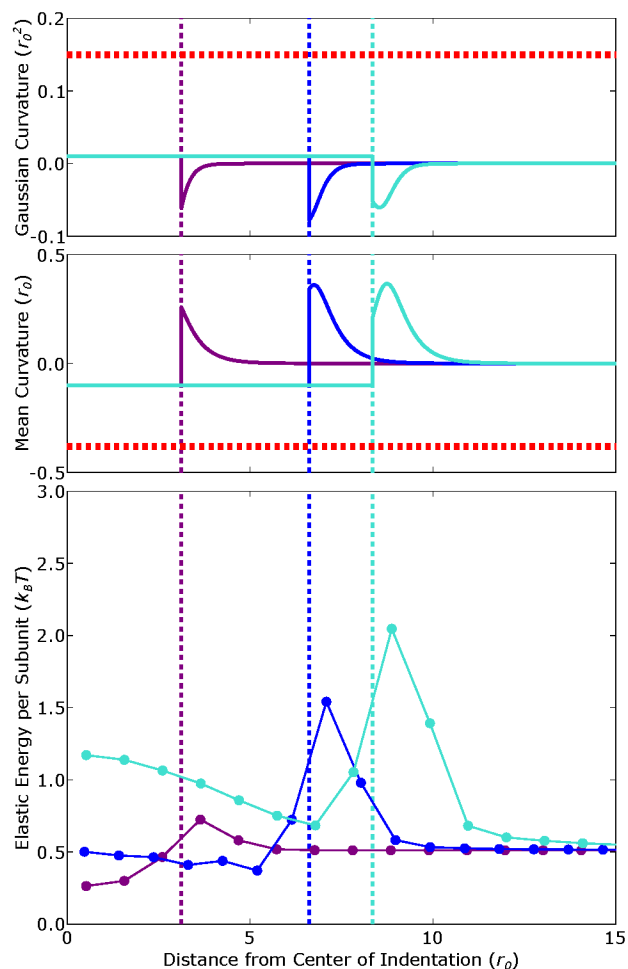
Fig. 3 *Top:* Solid lines show the Gaussian curvature of a membrane with $\sigma = 19k_BT/r_0^2$ in its ground state, with degree of indentation $f = 0.05$ (purple), $f = 0.25$ (blue), and $f = 0.45$ (turquoise). The vertical dashed lines represent the detachment radii and the horizontal dashed red line indicates the innate Gaussian curvature of a single clathrin subunit. *Middle:* Mean curvature of the ground state membrane configurations, and the inherent mean curvature of a model clathrin subunit. *Bottom:* Average elastic energy of clathrin subunits in their minimum energy configuration on such membranes, with a subunit elasticity of $k_s = 92.5k_BT/r_0^2$. Each dot represents the center of a concentric bin within which clathrin energies are averaged.

of $M_c = -0.38r_0^{-1}$. The large peaks in curvature are opposite in sign from this natural configuration, requiring an energetically costly distortion of hubs that are near the detachment point.

We quantify the extent of this curvature-driven distortion by finding the minimum energy configuration of crystalline lattices while associated to a membrane in its ground state, and examining how the elastic energy of individual subunits varies

with position. This calculation does not account for the effect of membrane or clathrin lattice fluctuations, but it does provide an estimate for the minimum elastic cost to a lattice as a result of the initial stages of nanoparticle wrapping. The minimum energy clathrin configurations are determined *via* simulated annealing of the clathrin with frozen bond connectivity on ground state membrane configurations that do not fluctuate. As part of the simulated annealing process, the clathrin connectivity is maintained in a perfectly satisfied honeycomb structure. The clathrin hub locations are initially free to fluctuate subject to Boltzmann acceptance probabilities at a temperature T_{max} that is 10 times higher than the physiological value T_{phys}. The temperature T is then reduced in stages, so that equilibrium can be reached in between reductions in T, from T_{max} to 0. Every 40 million steps, the temperature is reduced by a factor of 0.95. This repeats 167 times until the $T = 2 \times 10^{-4}T_{phys}$, and then 320 million steps of zero temperature steps are taken in which only negative energy changes are accepted.

Figure 3 shows the elastic energies of clathrin after simulated annealing, as a function of distance from the center of indentation. At all indentations, there is a noticeable peak in the elastic energies that corresponds to the regions of peaked curvature. This strain is accentuated at larger indentations, to the extent that the elastic energy near the detachment point is four times greater than its bulk value at $f = 0.45$. The circular scars in crystalline lattices with fluctuations that surround large deformations arise because the elastic costs of clathrin in that region become comparable to the marginal energetic benefit of binding a leg ($\varepsilon/2 = 3.25k_BT$). Unbinding of legs and subsequent generation of voids enables the relaxation of this costly energetic distortion. Snapshots of clathrin lattices at thermal equilibrium and in the completely connected ground state are shown in Fig. 4, with pinwheels colored according to their individual elastic energy. Even though the average energy at equlibrium is greater than in the ground state, this image shows how the distinct stress localization of perfectly connected lattices is somewhat alleviated when fluctuations and bond switching is allowed.

All of the results shown thus far have been representative of lattices that are crystalline in the quasi-flat case, and in these cases, orientational order persists outside of the highly indented regions despite a clustering of disorder within them. At different subunit elasticity or membrane tension, large indentations lead to melting of the surrounding bulk lattice into a fluid phase. Figure 5 shows snapshots of such systems at varying degrees of indentation. Above a certain indentation threshold that is specific to each system, the crystalline bulk phase loses its orientational order as it is populated with dense, decoupled defects. Thus, local clustering of defects can trigger propagation of disorder throughout the whole lattice.

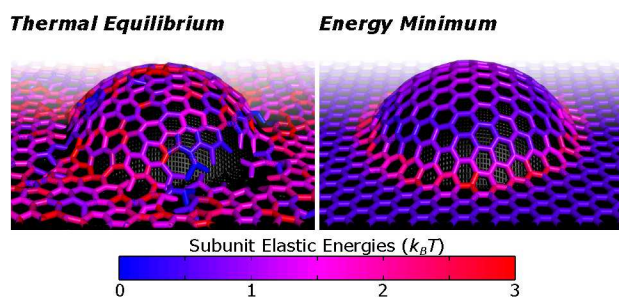Based on the broad range of tested parameter space, we de-

Fig. 4 Representative snapshots of clathrin configurations at thermal equilbrium and in their minimum energy configuration. Both images represent systems with $f = 0.45$, $\sigma = 19 k_B T / r_0^2$ and $k_s = 92.5 k_B T / r_0^2$. Individual subunits are colored based on their elastic energy, according to the scale given by the color bar.
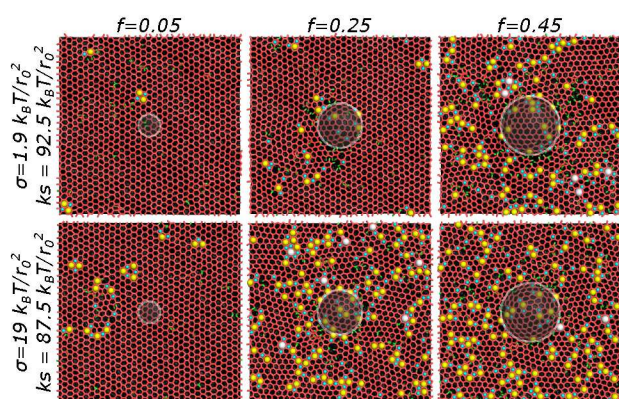

Fig. 5 Snapshots of our simulations with two distinct sets of physical parameters, separated in rows, and three different degrees of indentation, separated in columns. Coloring of clathrin, defects and indentations are the same as in Fig. 2.

Fig. 6 Phase diagrams of clathrin lattices, plotted as function of indentation and subunit elasticity. Each circle signifies a simulated parameter set, with the color of the circle corresponding to a specific membrane tension. Blue circles correspond to $\sigma = \infty$, red circles correspond to $\sigma = 19 k_B T / r_0^2$ and green circles correspond to $\sigma = 1.9 k_B T / r_0^2$. Empty circles represent crystalline equilibrium phases, while closed circles represent fluid phases. The dashed lines show approximate phase boundaries at each simulated tension. Thorough simulations were carried out in only the regions near the phase boundaries for each respective tension.

of the crystallinity threshold under quasiflat conditions. Indentations larger than $f = 0.45$ may spur a transition of these stiff lattices, but a more sophisticated membrane model would be required to adequately capture the membrane behavior.

4 Discussion

Our results demonstrate that ordered protein lattices on flexible membranes are profoundly affected by large deformations. This section begins with a physical explanation of how the membrane properties, the clathrin properties, and the nature of large-scale indentations conspire to determine the various lattice structures that are observed in our simulations. We then address the relevance of our findings to the biological function of clathrin assemblies based on *in vivo* observations.

Defect-mediated melting occurs when the elastic cost of decoupling dislocations is outweighed by the entropic benefit of the unpaired defect mobility[52]. In two-dimensional crystals, this tradeoff is determined by the in-plane stiffness of the lattice and the core energy of individual dislocations. The former is relatable to the stiffness of our model clathrin subunits[28], and the latter depends on the microscopic structure of our dislocations. KTHNY theory predicts that thermal fluctuations soften defect interactions and renormalize the bulk lattice stiffness to spur a melting transition at temperatures lower than those expected from bare physical parameters[52–54]. We observe this effect when simulating clathrin

termine a phase boundary for the indentation-based melting transition. Figure 6 illustrates how indentation, along with clathrin and membrane properties, influences the phase of the lattice as a whole. To concretely assess the phase of our simulated lattices, we measure the orientational order correlation function of our system, in a manner similar to that of Ref. [25], but with the center indented region excluded from our measurements. Crystalline phases are indicated by an orientational order correlation function that remains constant with distance between lattice points, while fluid phases are characterized by an exponential decay. Clathrin elasticity, when high enough, is capable of enforcing a crystalline phase at all tensions. The phase boundary between crystalline and fluid phases exists at a higher subunit elasticity for lower tensions, reflecting work done in Refs.[25] and[28]. When close to this boundary, large indentations of a crystalline phase can drive a transition to a fluid phase. We do not observe any phase transitions for subunit elasticities that are more than 10% greater than the value
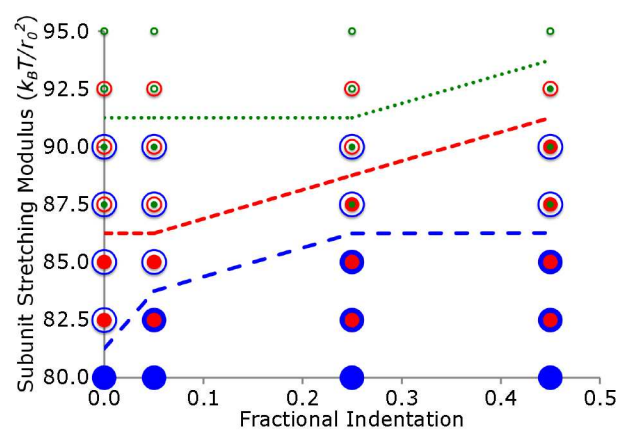
systems in purely two dimensions [28], bolstering our justification for analyzing model clathrin lattices through the lens of defect mediated melting. When the surface underlying an ordered crystal is deformable, lone dislocations are stabilized by localized out-of-plane buckling, which enables melting of lattices that would otherwise remain crystalline on a flat surface [57,58]. However, the existence of a finite tension can counteract this melting mechanism by suppressing out-of-plane deformations [25,59]. Out-of-plane membrane fluctuations also play an important role, as they tend to lower the melting temperature of a supported two-dimensional crystal [57,60,61].

For ordered crystals that are constrained to surfaces of fixed non-zero curvature, such as our systems exhibiting indentation, the energetics of defects and their coupling to one another depend strongly on the topology and local curvature of the surface [62]. In the ground state, certain defects are localized to certain regions of surfaces through a geometric potential that is dependent on the Gaussian curvature [63–65]. The "Gaussian bump" [65–67] is a type of surface deformation whose impact on associated 2D crystals has been previously studied. This structure is similar to our spherical cap indentation in that it is an axially symmetric deformation defined by a central rounded protrusion. Unlike the Gaussian bump, our indented membranes exhibit sharp changes in curvature near the detachment points as a response to tension (see Fig. 3), but the fundamentally similar nature of these two surfaces warrants comparison. Models of 2D crystals on Gaussian bumps have shown that decoupled dislocations and disclinations can effectively alleviate frustration in the crystal when localized to specific regions [65–67]. The energetic benefit of these lone dislocations is only achieved when the bump exceeds some critical aspect ratio ξ_c, which depends on the lattice properties and the width of the bump [65,66]. Indeed, the aspect ratio ξ of our own indentations approximately exceeds ξ_c only when $f \geq 0.25$, corresponding to the fractional indentations that elicit localized defects or bulk phase transitions.

Several attributes of our model result in distinct physical behavior that is not typical in the aforementioned 2D crystal systems. The clathrin pucker angle α_0 effectively introduces a geometric coupling between the triskelia and the membrane shape, with each subunit preferring a sharply positive Gaussian curvature ($K_c = 0.15r_0^{-2}$) and a sharply negative mean curvature ($M_c = -0.38r_0^{-1}$) relative to the peaks exhibited in our system. These mismatches in curvature result in a preponderance of defects and void spaces in the regions surrounding the detachment points. The localization of void spaces in particular near high-curvature regions results from the specific leg-leg bonds that mediate interactions between our subunits. Unlike in fixed-connectivity models or soft interaction models (*e.g.* Yukawa pair potentials [67]), high local elastic stresses can be relaxed by the dissociation of specific bonds, which leads to delocalization of clathrin away from regions of high curva-

ture. The resulting voids sharply reduce the additional elastic strain introduced by nearby lone dislocations or disclinations, enabling the indentation-induced phase transitions that are shown in many of our numerical simulations.

Clathrin coats stabilize highly curved vesicles *in vivo* by aggregating into large interconnected structures [6,68,69]. The exact origin of membrane curvature and its effect on the function of these large arrays of proteins is still unresolved. Many proteins are known to drive membrane curvature through insertion or scaffolding mechanisms [70,71], but there is also evidence that membrane curvature itself contributes to the localization and activity of certain associated proteins [72–75]. For example, cell surfaces impinged by 200 nm nanocones have exhibited elevated levels of both clathrin and amphiphysin, a curvature-associated protein responsible for recruiting molecules that enable vesicle scission [75]. Despite the clear localization of these endocytic components, there was no observed increase in endocytic activity on the impinged regions relative to cell surfaces on flat glass. Nonetheless, other studies have shown increased molecular uptake induced by nanowires of comparatively large aspect ratio, raising the possibility that external deformations are capable of driving heightened endocytic activity [22–24]. All of these deformations are induced on basal cell surfaces, which are likely to contain clathrin plaques, but there has yet to be a detailed assessment of the frequency with which external impingements interact with plaques in particular. By enforcing curvature through a fixed spherical indentation in our simulations, we explicitly demonstrate a transformation from plaque-like clathrin lattices to fluid states amenable to pit formation as a physical response to membrane deformations.

Large, flat clathrin plaques similar to our simulated lattices exist in living cells, but their relation to endocytic vesicle formation is somewhat unclear [10]. Plaques are capable of slowly internalizing through an actin-dependent mechanism that is energetically costly compared to canonical clathrin pit internalization [8–10]. Electron microscopy snapshots appear to show curved pits budding off of plaques [11,12], and *in vitro* systems of large clathrin lattices on liposomes form spherical buds upon heating [15]. Additionally, certain cargo and adaptor proteins can induce large clathrin coated structures from which CCV's bud off, leaving behind a residual clathrin patch [76]. These findings suggest that clathrin subunits within plaques may occasionally rearrange to form pit-like structures suitable for vesiculation and internalization.

Our work suggests a possible pathway that clathrin lattices can take in transforming from flat plaques to curved pits. Above a certain degree of indentation, the imposed curvature on our model membrane acts to disrupt the ordered honeycomb structure of the lattice by breaking bonds and forming localized defects, occasionally driving the lattice into the fluid state. When clathrin are unbound or within a fluid lattice, they can more easily reorganize into pit-like assemblies that ac-

commodate curved shapes. These assemblies include isolated defects such as 5-sided rings that are energetically unfavorable in flat plaques but topologically required for closed vesicle formation[55], a necessary step in endocytosis. This physical pathway may be at work when nanowire indentations cause localized heightened delivery of biomolecules into cells[22] without directly puncturing the cell membranes[23,24].

5 Conclusions

Our numerical simulations demonstrate that crystalline protein order on flexible fluctuating membranes is dramatically influenced by local deformations. In very rigid lattices, defects and void spaces are localized to the region of deformation, while similar deformations on a lattice with a lower stiffness causes melting to a fluid phase of the entire surrounding system. These observations are consistent with previous studies of ordered systems on curved, flexible surfaces that identify a coupling between membrane curvature and defects in crystals.

We therefore identify a physical mechanism by which clathrin plaques on cell membranes respond to local membrane curvatures in a manner that enhances endocytosis. The disruption of lattices by localized deformations enables large-scale lattice reorganization into budding pits that can then efficiently internalize cargo. Our theoretical findings have direct applications to recent experimental observations, and can guide the development of future technologies that rely on intracellular transport.

6 Appendix A: Clathrin Model

We use the same model for our clathrin triskelia as that which is published in Ref.[25], and we present a summary of that model in this appendix. Each clathrin triskelion is represented as a three-legged pinwheel. Any unbound leg is capable of forming a bond with an unbound leg of another triskelion, causing a reduction in energy equal to ε. Bound pairs of legs may also unbind. When clathrin are bound to one another, deformations away from their minimum energy configuration incurs elastic stresses on the structure through four harmonic modes, which are illustrated in Fig. 1.

The total energy of a collection of N pinwheels in our model

is given by

$$
\begin{aligned}
E_{clath} = &- \varepsilon \sum_{i=1}^{N-1} \sum_{j=i+1}^{N} L_{ij} + k_r \sum_{i=1}^{N-1} \sum_{j=i+1}^{N} V\left(d - r_{ij}\right) \left[\left(\frac{d}{r_{ij}}\right)^4 - 1 \right] \\
&+ \frac{k_s}{2} \sum_{i=1}^{N-1} \sum_{j=i+1}^{N} \left(r_{ij} - r_0\right)^2 L_{ij} + \frac{k_t}{2} \sum_{i=1}^{N-1} \sum_{j=i+1}^{N} \gamma_{ij}^2 L_{ij} \\
&+ \frac{k_b}{2} \sum_{i=1}^{N} \sum_{j=1}^{N-1} \sum_{k=j+1}^{N} \chi_i^{jk}\left(\lambda_i^j, \lambda_i^k, \lambda_i^l\right) L_{ij} L_{ik} \\
&+ \frac{k_o}{2} \sum_{i=1}^{N} \sum_{j=1}^{N} \left(\alpha_i^j - \alpha_0\right)^2 L_{ij},
\end{aligned}
\tag{2}
$$

where the state of pinwheel i is fully defined by its hub's position $\vec{r}_i$, its normal vector $\vec{n}_i$, and the bond connectivity of its three legs. The bond connectivity is fully characterized by the link indicators L_{ij} and the leg index indicators λ_i^j for all the hub indices j of the other pinwheels in the model. If hubs i and j are bound, then $L_{ij} = 1$, whereas if they are unbound, then $L_{ij} = 0$. The leg index indicator λ_i^j gives the leg index (between 1 and 3) of the leg on hub i that connects to hub j, and $\lambda_i^j = 0$ if $L_{ij} = 0$.

A hard core potential is modulated by the repulsive strength k_r, which is set to $1 k_B T$. It imposes steric limitations on the locations of the hubs, and is activated between hubs i and j by the Heaviside step function $V(x)$ only when the separation between the two is less than a cutoff distance d, which is set to $0.8 r_0$. The stretching modulus, k_s, resists elongation or compression of the inter-hub bonds relative to their equilibrium length, r_0, and the twisting modulus k_t, resists torsion of these bonds. The in-plane bending modulus k_b resists distortion of the legs beyond a uniform radial distribution when projected onto their normal plane, through a Hookean angular spring whose exact form χ_i^{jk} depends on the bond connectivity. The out-of-plane bending modulus, k_o resists deformation of the triskelion's pucker angle away from an intrinsic value α_0, with an unpuckered, planar clathrin structure corresponds to $\alpha_0 = 90°$. Ref.[25] includes a more detailed mathematical formulation of this model.

7 Appendix B: Membrane Ground State With Indentation

Because we test only modest degrees of indentation resulting in small gradients, the membrane ground state is determined by setting linear order functional variations of E_{mem} with respect to h equal to zero. Starting from Eqn 1, this gives the differential equation

$$
\nabla^2 \left(\nabla^2 h - \frac{h}{L_c} \right) = 0.
\tag{3}
$$

The solution to Eq. 3, along with the membrane adherence to the nanoparticle inside the radial coordinate of the detachment point ρ_0, gives the complete axially symmetric ground state height profile of the membranes. Using the reference point $h(\rho_0) = 0$ and with $\rho = 0$ at the center of the indentation, this profile is

$$h(\rho) = \begin{cases} \sqrt{R_N^2 - \rho^2} - \sqrt{R_N^2 - \rho_0^2} & \text{if } \rho < \rho_0 \\ A\left[K_0(\rho/L_c) - K_0(\rho_o/L_c)\right] & \text{if } \rho \geq \rho_0, \end{cases} \quad (4)$$

with

$$A \equiv \frac{L_c \rho_0}{\sqrt{R_N^2 - \rho_0^2} K_1(\rho_0/L_c)}.$$

K_0 and K_1 are 0th and 1st order modified Bessel functions of the second kind.

To appropriately adjust our simulation boundaries so that clathrin density is constant, we calculate the surface area within the area confined by the original boundaries ($A_0 = L_{x0}L_{y0}$) using

$$A_{s0} = \iint\limits_{A_0} d\vec{\rho} \sqrt{1 + \left(\vec{\nabla}h(\vec{\rho})\right)^2}. \quad (5)$$

The region with excess surface area relative to the flat case is contained well within a circular region of radius L_{x0} for all our parameter sets, allowing us to evaluate Eq. 5 using polar coordinates over this region only instead of over the square cell. The integral is separated into an inner portion for $\rho < \rho_0$ that is analytically simple, and an outer outer portion for $\rho_0 < \rho \leq L_{x0}$ that we integrate numerically. The excess area is then given by $\Delta A = A_{s0} - \pi L_{x0}^2$, and the appropriate simulation boundaries L_x and L_y are then given by the solutions to the two equations

$$\begin{aligned} L_x L_y &= L_{x0}L_{y0} - \Delta A \\ \frac{L_x}{L_y} &= \frac{L_{x0}}{L_{y0}}. \end{aligned} \quad (6)$$

The Gaussian curvature K of gently curved axially symmetric configurations is defined in polar coordinates as

$$K(\rho) = \frac{h_{\rho\rho}h_\rho}{\rho\left(1+h_\rho^2\right)^2}, \quad (7)$$

where h_ρ and $h_{\rho\rho}$ are the first and second derivatives of the height field with respect to the radial coordinate ρ, repectively. Making the variable substitutions $z \equiv \rho/L_c$ and $z_0 \equiv \rho_0/L_c$ gives the result,

$$K(z) = \begin{cases} R_N^{-2} & \text{if } z < z_0 \\ \dfrac{-\left(A^2/L_c^4\right)K_1(z)\left[K_0(z)+z^{-1}K_1(z)\right]}{z\left[1+(A/L_c)^2K_1^2(z)\right]^2} & \text{if } z \geq z_0, \end{cases} \quad (8)$$

that is plotted with respect to ρ in Fig. 3. The mean curvature M is defined by

$$M(\rho) = \frac{h_{\rho\rho} + \rho^{-1}\left(h_\rho + h_\rho^3\right)}{2\left(1+h_\rho^2\right)^{3/2}}, \quad (9)$$

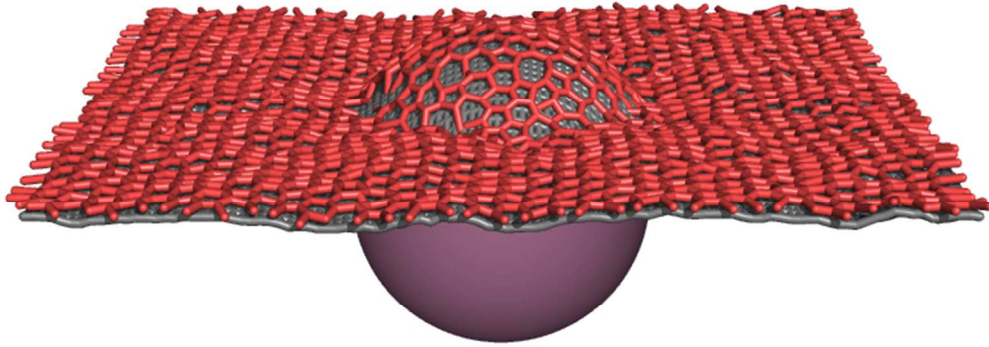resulting in the two-part equation that is also plotted in Fig 3:

$$M(z) = \begin{cases} R_N^{-1} & \text{if } z < z_0 \\ \dfrac{A\left[L_c^2 z K_0(z) - A^2 K_1^2(z)\right]}{L_c z\left[L_c^2 + A^2 K_1^2(z)\right]^{3/2}} & \text{if } z \geq z_0. \end{cases} \quad (10)$$

References

1 H. T. McMahon and E. Boucrot, *Nature Reviews: Molecular Cell Biology*, 2011, **12**, 517–33.

2 F. M. Brodsky, *Annual Review of Cell and Developmental Biology*, 2012, **28**, 309–36.

3 T. Roth and K. Porter, *The Journal of Cell Biology*, 1964, 313–332.

4 T. Kanaseki and K. Kadota, *The Journal of Cell Biology*, 1969, **42**, 202–220.

5 B. M. Pearse, *Journal of Molecular Biology*, 1975, **97**, 93–8.

6 L. Hinrichsen, A. Meyerholz, S. Groos and E. J. Ungewickell, *Proceedings of the National Academy of Sciences of the United States of America*, 2006, **103**, 8715–20.

7 E. Cocucci, F. Aguet, S. Boulant and T. Kirchhausen, *Cell*, 2012, **150**, 495–507.

8 C. J. Merrifield, D. Perrais and D. Zenisek, *Cell*, 2005, **121**, 593–606.

9 K. D. Bellve, D. Leonard, C. Standley, L. M. Lifshitz, R. A. Tuft, A. Hayakawa, S. Corvera and K. E. Fogarty, *The Journal of Biological Chemistry*, 2006, **281**, 16139–16146.

10 S. Saffarian, E. Cocucci and T. Kirchhausen, *PLoS Biology*, 2009, **7**, e1000191.

11 J. Heuser, J. Keen, L. Amende, R. Lippoldt and K. Prasad, *The Journal of Cell Biology*, 1987, **105**, 1999–2009.

12 L. M. Fujimoto, R. Roth, J. E. Heuser and S. L. Schmid, *Traffic*, 2000, **1**, 161–71.

13 L. M. Traub, *PLoS biology*, 2009, **7**, e1000192.

14 W. K. den Otter and W. J. Briels, *Traffic (Copenhagen, Denmark)*, 2011, **12**, 1407–16.

15 P. N. Dannhauser and E. J. Ungewickell, *Nature Cell Biology*, 2012, **14**, 634–9.

16 C. Bazinet, A. Katzen, M. Morgan, A. Mahowald and S. Lemmon, *Genetics*, 1993, **134**, 1119–1134.

17 T. Inoue, T. Hayashi, K. Takechi and K. Agata, *Development*, 2007, **134**, 1679–89.

18 S. Agarwal, R. Rastogi, D. Gupta, N. Patel, M. Raje and A. Mukhopadhyay, *Biochimica et Biophysica Acta*, 2013, **1833**, 1065–1077.

19 A. C. Humphries and M. Way, *Nature Reviews Microbiology*, 2013, **11**, 551–560.

20 I. Mellman and Y. Yarden, *Cold Spring Harbor perspectives in biology*, 2013, **5**, a016949.

21 A. Yu, Y. Shibata, B. Shah, B. Calamini, D. C. Lo and R. I. Morimoto, *Proceedings of the National Academy of Sciences*, 2014, 1–10.

22 A. K. Shalek, J. T. Robinson, E. S. Karp, J. S. Lee, D.-R. Ahn, M.-H. Yoon, A. Sutton, M. Jorgolli, R. S. Gertner, T. S. Gujral, G. MacBeath, E. G. Yang and H. Park, *Proceedings of the National Academy of Sciences of the United States of America*, 2010, **107**, 1870–5.

23 X. Xie, A. M. Xu, M. R. Angle, N. Tayebi, P. Verma and N. a. Melosh, *Nano letters*, 2013, **13**, 6002–8.

24 A. M. Xu, A. Aalipour, S. Leal-Ortiz, A. H. Mekhdjian, X. Xie, A. R. Dunn, C. C. Garner and N. A. Melosh, *Nature communications*, 2014, **5**, 3613.

25 N. Cordella, T. J. Lampo, S. Mehraeen and A. J. Spakowitz, *Biophysical Journal*, 2014, **106**, 1476–1488.

26 T. Kirchhausen and S. C. Harrison, *Cell*, 1981, **23**, 755–61.

27 A. Fotin, Y. Cheng, P. Sliz, N. Grigorieff, S. C. Harrison, T. Kirchhausen and T. Walz, *Nature*, 2004, **432**, 573–9.

28 S. Mehraeen, N. Cordella, J. S. Yoo and A. J. Spakowitz, *Soft Matter*, 2011, **7**, 8789.

29 A. P. Schoen, N. Cordella, S. Mehraeen, M. A. Arunagirinathan, A. J. Spakowitz and S. C. Heilshorn, *Soft Matter*, 2013, **9**, 9137–9145.

30 M. L. Ferguson, K. Prasad, D. L. Sackett, H. Boukari, E. M. Lafer and R. Nossal, *Biochemistry*, 2006, **45**, 5916–22.

31 A. Musacchio, C. J. Smith, A. M. Roseman, S. C. Harrison, T. Kirchhausen and B. M. Pearse, *Molecular Cell*, 1999, **3**, 761–70.

32 J. Heuser and T. Kirchhausen, *Journal of Ultrastructure Research*, 1985, **92**, 1–27.

33 Shafigh Mehraeen, *Ph.D.*, Stanford University, 2011.

34 R. Goetz, G. Gompper and R. Lipowsky, *Physical Review Letters*, 1999, **82**, 221–224.

35 E. Lindahl and O. Edholm, *Biophysical Journal*, 2000, **79**, 426–33.

36 M. C. Wiener and S. H. White, *Biophysical Journal*, 1992, **61**, 434–47.

37 P. B. Canham, *Journal of Theoretical Biology*, 1970, **26**, 61–81.

38 W. Helfrich, *Zeitschrift fur Naturforschung C*, 1973, **28**, 693–703.

39 F. L. H. Brown, *Annual Review of Physical Chemistry*, 2008, **59**, 685–712.

40 M. Ehrlich, W. Boll, A. Van Oijen, R. Hariharan, K. Chandran, M. L. Nibert and T. Kirchhausen, *Cell*, 2004, **118**, 591–605.

41 H. McMahon, *Current biology*, 1999, **9**, R332–R335.

42 P. Cossart and P. J. Sansonetti, *Science (New York, N.Y.)*, 2004, **304**, 242–8.

43 E. Veiga, J. A. Guttman, M. Bonazzi, E. Boucrot, A. Toledo-Arana, A. E. Lin, J. Enninga, J. Pizarro-Cerdá, B. B. Finlay, T. Kirchhausen and P. Cossart, *Cell host & microbe*, 2007, **2**, 340–51.

44 E. Moreno-Ruiz, M. Galán-Díez, W. Zhu, E. Fernández-Ruiz, C. D'Enfert, S. G. Filler, P. Cossart and E. Veiga, *Cellular microbiology*, 2009, **11**, 1179–89.

45 D. K. Cureton, R. H. Massol, S. Saffarian, T. L. Kirchhausen and S. P. J. Whelan, *PLoS pathogens*, 2009, **5**, e1000394.

46 M. Deserno and T. Bickel, *Europhysics Letters (EPL)*, 2003, **62**, 767–774.

47 M. Deserno, *Physical Review E*, 2004, **69**, 031903.

48 C. Morris and U. Homann, *Journal of Membrane Biology*, 2001, **179**, 79–102.

49 N. Metropolis, A. W. Rosenbluth, M. N. Rosenbluth, A. H. Teller and E. Teller, *The Journal of Chemical Physics*, 1953, **21**, 1087–1092.

50 J. E. Heuser, J. H. Keen, L. M. Amende, R. E. Lippoldt and K. Prasad, *The Journal of cell biology*, 1987, **105**, 1999–2009.

51 J. Heuser, *The Journal of Cell Biology*, 1989, **108**, 401–11.

52 J. M. Kosterlitz and D. J. Thouless, *Journal of Physics C: Solid State*, 1973, **6**, 1181–1203.

53 D. Nelson and B. Halperin, *Physical Review B*, 1979, **19**, 2457–2484.

54 A. Young, *Physical Review B*, 1979, **19**, 1855–1866.

55 D. S. Richeson, *Euler's Gem: The Polyhedron Formula and the Birth of Topology*, Princeton University Press, Princeton, NJ, 2008.

56 E. Kocsis, B. L. Trus, C. J. Steer, M. E. Bisher and A. C. Steven, *Journal of Structural Biology*, 1991, **107**, 6–14.

57 D. Nelson and L. Peliti, *Journal de Physique*, 1987, **48**, 1085–1092.

58 H. S. Seung and D. R. Nelson, *Physical Review A*, 1988, **38**, 1005–1018.

59 D. Morse and T. Lubensky, *Journal de Physique II*, 1993, **3**, 531–546.

60 J. Aronovitz and T. Lubensky, *Physical Review Letters*, 1988, **60**, 2634–2637.

61 P. Le Doussal and L. Radzihovsky, *Physical Review Letters*, 1992, **69**, 1209–1212.

62 M. J. Bowick and L. Giomi, *Advances in Physics*, 2009, **58**, 449–563.

63 S. Sachdev and D. Nelson, *Journal of Physics C: Solid State . . .* , 1984, **17**, 5473–5489.

64 M. Bowick, D. Nelson and A. Travesset, *Physical Review B*, 2000, **62**, 8738–8751.

65 V. Vitelli, J. B. Lucks and D. R. Nelson, *Proceedings of the National Academy of Sciences of the United States of America*, 2006, **103**, 12323–8.

66 V. Vitelli and A. Turner, *Physical Review Letters*, 2004, **93**, 19–22.

67 A. Hexemer, V. Vitelli, E. Kramer and G. Fredrickson, *Physical Review E*, 2007, **76**, 1–12.

68 A. Jin and R. Nossal, *Biophysical Journal*, 2000, **78**, 1183–94.

69 R. Nossal, *Traffic (Copenhagen, Denmark)*, 2001, **2**, 138–47.

70 M. G. J. Ford, I. G. Mills, B. J. Peter, Y. Vallis, G. J. K. Praefcke, P. R. Evans and H. T. McMahon, *Nature*, 2002, **419**, 361–6.

71 A. Frost, R. Perera, A. Roux, K. Spasov, O. Destaing, E. H. Egelman, P. De Camilli and V. M. Unger, *Cell*, 2008, **132**, 807–817.

72 R. Lundmark, G. J. Doherty, Y. Vallis, B. J. Peter and H. T. McMahon, *The Biochemical journal*, 2008, **414**, 189–94.

73 J. Liu, Y. Sun, D. G. Drubin and G. F. Oster, *PLoS biology*, 2009, **7**, e1000204.

74 J. Liu, Y. Sun, G. F. Oster and D. G. Drubin, *Current opinion in cell biology*, 2010, **22**, 36–43.

75 M. Galic, S. Jeong, F.-C. Tsai, L.-M. Joubert, Y. I. Wu, K. M. Hahn, Y. Cui and T. Meyer, *Nature cell biology*, 2012, **14**, 874–81.

76 M. Mettlen, D. Loerke, D. Yarar, G. Danuser and S. L. Schmid, *The Journal of cell biology*, 2010, **188**, 919–33.

273x224mm (72 x 72 DPI)